LAWRENCE
LIVERMORE
NATIONAL
LABORATORY

LLNL-PROC-411719

Towards Next Generation TATB-based Explosives by Understanding Voids and Microstructure from 10 nm to 1 cm

T. M. Willey, G. Overturf

April 1, 2009

40th International Annual Conference of ICT
Karlsruhe, Germany
June 23, 2009 through June 26, 2009

Disclaimer

TOWARDS NEXT GENERATION TATB-BASED EXPLOSIVES BY UNDERSTANDING VOIDS AND MICROSTRUCTURE FROM 10 NM TO 1 CM

Trevor M. Willey and George E. Overturf
Lawrence Livermore National Laboratory, 7000 East Ave, Livermore CA, USA

TATB-based explosives have been investigated on length scales spanning several orders of magnitude, from just under 10 nm to larger than 1 cm. This has been accomplished using a combination of ultra-small angle x-ray scattering (USAXS), ultra-small angle neutron scattering (USANS), and x-ray computed tomography (XRCT). USAXS determines distributions the smallest structures including hot-spot voids from hundreds of nanometers to a few microns, USANS extends this range to about 10 microns, and two variants of XRCT cover sizes from microns to centimeters. Several examples are presented for LX-17, a triaminotrinitrobenzene based plastic bonded explosive using Kel-F 800. As an extension of previous USAXS results, in these proceedings, an alternate binder results in a more uniform microstructure for the PBX, useful towards design of next-generation TATB-based explosives. These data are an important step to understanding microstructural mechanisms that affect the mechanical properties of TATB-based explosives, and provide complete a comprehensive characterization of the structure of LX-17 from nanometers to centimeters that can be used as empirical input to computational models of detonation, and in determining the relationship between voids and microstructure to detonation properties.

Introduction

The nano-, meso-, and microstructure of insensitive plastically bonded explosives (PBXs) are of fundamental importance to understand both the mechanical properties and the relationship between structure and detonation properties of these materials. This proceeding presents an overview of several techniques to investigate structure over size ranges from a few nanometers to a few centimeters. Several examples of how these various techniques can be used to investigate triaminotrinitrobenzene (TATB) based explosives will be presented.

To comprehensively cover size regimes of interest, small-angle x-ray and neutron scattering techniques and x-ray computed tomography (XRCT) have been used. Each of these approaches gives information on different and complementary length scales. Ultra-small angle x-ray scattering (USAXS) can determine structural inhomogeneities arising from a minority phase (in this case the minority phase is void)[1] from a few nanometers to a few microns. Ultra-small angle neutron scattering (USANS) bridges the gap between USAXS and imaging techniques, and extends the sensitivity of scattering to about 10 microns. X-ray tomography can now routinely probe below 1 micron; we have used the imaging system incorporated in a focused ion beam (FIB) instrument, denoted XRCT, FIB in this work. Finally, synchrotron-based x-ray microtomography allows imaging of low-z materials with reasonable contrast from a few microns to about 1 cm. These techniques and their capabilities are summarized in Figure 1.

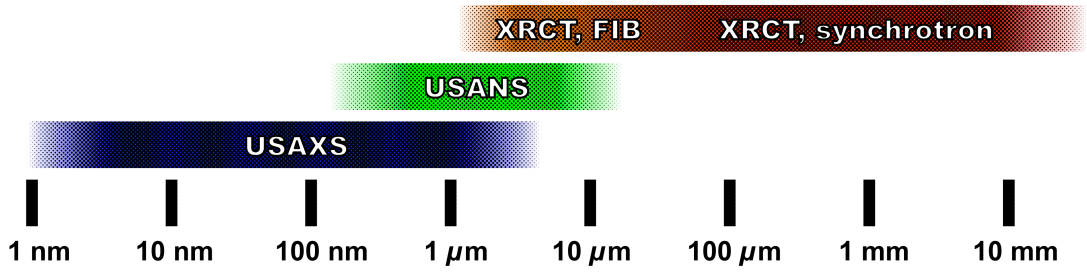

Figure 1: Techniques that have been used to comprehensively characterize TATB-based explosives, with size regimes over six orders of magnitude.

USAXS has been used to study void distributions within TATB-based explosives[1, 2]. Hot-spot models predict that voids on the order of 100 nm to 1 μm affect initiation and detonation properties[3-5]. Experimental determination of void size distributions covering these sizes is thus essential feedback to both hot-spot theory and to experimentally determine the relationship between void-size distributions and detonation properties.

TATB-explosives are also prone to an irreversible volume expansion with temperature cycling, commonly known as "ratchet growth". In general, various TATB-based explosives have log-normal distributions, that during the warm portion of the temperature cycle, increase in void volume and mean void size[1, 2]. Binders with higher glass transition temperature (T_g) can reduce the volume expansion[6, 7], but the wetting and adhesion of these binders is also critical to minimizing ratchet growth[2, 8, 9]. Understanding mechanisms for ratchet growth allows future choice of explosive/binder mixtures to minimize these types of changes, further extending PBX shelf-life.

USAXS does not comprehensively cover all of the void sizes; there is discrepancy between the USAXS-derived void volume and the physically measured density. In LX-17 and PBX-9502, PBX's containing TATB and Kel-F 800 binder, before ratchet growth, USAXS accounts for about 75-80% of the voids, while after ratchet growth, USAXS accounts for about 65% of the voids[1]. The deviation from a 1:1 correlation with density indicates the existence and creation of voids with dimensions larger than a few microns.

USANS, with scattering vector approaching 10^{-5} $Å^{-1}$ can probe slightly larger structures than USAXS to about 10 μm. In this proceeding, we show that USANS accounts for some, but not all of these "missing" voids. We will present USAXS data for completeness as well as the USANS data.

At larger sizes, TATB explosives with Kel-F 800 binder exhibit heterogeneous microstructure[10], and also exhibit two classes of larger voids that account for the balance of void volume not probed by USAXS and USANS. We will present our current work on determining size distributions of these larger voids, and our hypotheses on how these larger voids form during processing using x-ray computed tomography. Finally, we will show how new processing techniques and binders can produce a more homogenous mictrostructure in TATB –based explosives.

Experimental

LX-17 (nominally 92.5% TATB and 7.5% Kel-F 800 binder) and TATB/Cytop A samples were prepared as outlined previously[1, 2], with the following exceptions. The samples for USANS and USAXS were pressed to about 1.5 mm thick. The FIB XRCT samples were pressed to 0.8 mm thick, and then cut with a femtosecond laser[11] to obtain 0.4 mm diameter, 0.8 mm long cylinders. For synchrotron-based tomography studies of microstructure, LX-17 samples were pressed into 1.27 cm diameter, 2.54 cm long cylinder samples. Densities of 1.91 to 1.92 g/ cm^3 were obtained by pressing three times at 2.1 x 10^8

Pa (3.0 x 10^4 PSI) for 5 minutes each press, with the pressing die held at 105° C. Using two instead of three pressings resulted in a sample of 1.89 g/cm^3.

The USAXS data were acquired using beam line 32-ID at the Advanced Photon Source, Argonne National Laboratory, Argonne, Illinois, U.S.A.[12-14] The endstation includes a Bonse-Hart camera, which can measure scattering vectors (q) from about 10^{-4} $Å^{-1}$ to 1 $Å^{-1}$. The monochromator was positioned at about 11 keV (1.13 Å). Data were processed using the codes developed for use on this USAXS instrument, and included absolute scattering intensity calibration and slit desmearing.

USANS measurements were performed at the Perfect Crystal Diffractometer for Ultra Small-Angle Neutron Scattering at the National Center for Neutron Research, National Institute of Standards and Technology, Gaithersburg, Maryland[15, 16]. Data were acquired on samples mounted in Cd windows 1.59 cm in diameter, and were reduced using the integrated software package[16].

Inhomogeneities in electron density (USAXS) or nuclear makeup and density (USANS) give rise to small angle x-ray scattering. The scattering contrast between TATB and Kel-F 800 binder is minimal: for 11 keV x-rays, the contrasts are about 16.6 x 10^{10} cm^{-2} for TATB and 17.5 x 10^{10} cm^{-2} for Kel-F 800, and for the neutrons, the contrast is about 4.9 x 10^{10} cm^{-2} and 4.4 x 10^{10} cm^{-2} for TATB and Kel-F 800 respectively. Thus, voids are the primary source of scattering. Although the scattering contrast difference between TATB and Kel-F 800 is larger with neutrons than with x-rays, the contrast still similar enough to conclude that voids are the main cause of scattering. In fact, if one assumes the neutron scattering in LX-17 comes from the minority Kel-F 800 phase, rather than voids, using the scattering contrast between TATB and Kel-F 800, an unphysical result for the Kel-F volume fraction (>45%) ensues. Void size distributions, assuming uncorrelated voids, were derived from the scattering using the maximum entropy method, implemented in the *Irena* package for SAS data analysis[17]. The implementation for TATB-based explosives has been described previously[1, 2].

High-resolution tomography was performed using an instrument designed primarily for Focused Ion Beam (FIB) processes. The x-ray tomography portion of the instrument is a point projection SEM hosted x-ray system, with an electron beam spot size of ~2 nm using an electron gun energy of 20 kilovolts, and a platinum target with a prominent K-line at 9.44 keV. The images were recorded on a 1340 x 1300 CCD array with pixel size of 20 by 20 microns. The source to detector distance was 211 mm, while the source to sample distance was set to 2.64 millimeters, leading to camera pixels representing about 0.25 by 0.25 microns

each at the CCD detector. Views were acquired at 1-degree increments through 360 degrees. The reconstruction was performed using proprietary software provided by the manufacturer (Gatan, Inc., Pleasanton, California).

The presented synchrotron based tomography data were acquired at beamline 8.3.2 at the Advanced Light Source, Lawrence Berkeley National Laboratory[18], using a photon energy of 20 keV. Every 20 views, bright field images were acquired to normalize incident x-ray flux and the decay in the synchrotron storage ring source current; dark field images were also acquired. The transmitted x-rays impinge upon a $CdWO_4$ single crystal scintillator, and are recorded by a Cooke PCO 4000 CCD camera. In order to minimize phase effects, the camera and scintillator box are moved as close as possible to the specimen. Auxillary data were also acquired at beamline BM2 at the Advanced Light Source[19].

Tomographic slices were reconstructed via filtered backprojection using the LLNL-developed *ImageRec* code to retrieve attenuation coefficients μ in units of mm^{-1} for each voxel within the volume. Attenuation of x-rays through a specimen is described by $I = I_0 e^{-\mu x}$ where I is the x-ray intensity through a material, I_0 is the initial x-ray intensity, x is the material thickness, and μ is an attenuation coefficient characteristic of the material and dependent upon density. In order to remove ring artifacts from each sinogram, each row was fit with the attenuation expected from a cylinder, and the rows and fits were averaged. This allowed for deconvolution of the x-ray attenuation through the part from artifacts introduced by the detector, scintillator, camera optics, and by inhomogeneous x-ray illumination.

Results and Discussion

Figure 2 presents both the USAXS and the USANS scattering on LX-17 before and after temperature cycling, on the exact same set of two samples. The cycling produces a distinct change in the scattering associated with ratchet growth. The USAXS is sensitive to structures from a few nm to a few microns, while USANS can reach nearly one order of magnitude lower in scattering angle, and can thus probe structures up to nearly 10 microns. The Gunier region in both pre- and post-ratchet specimens is well defined in the USANS. This already indicates that structures at or slightly larger than 10 microns are not prevalent in these samples. To gain a more quantitative estimate of the void sizes, maximum entropy methods[17] were used to derive void size distributions. These distributions are presented in figure 3.

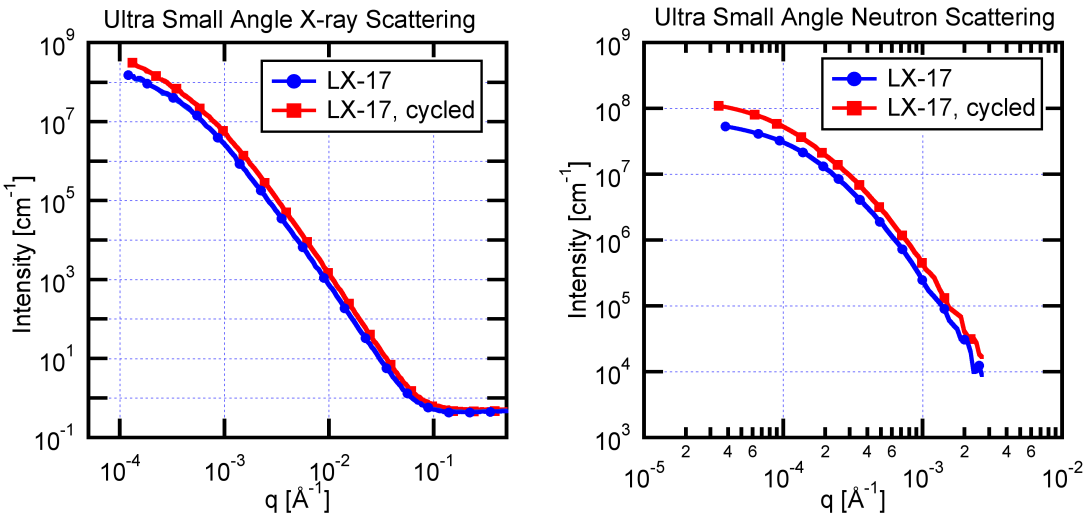

Figure 2: Left pane: Ultra small-angle x-ray scattering profile of LX-17; pristinely pressed (circles) and after temperature cycling (squares.) Right pane: On exactly the same samples, ultra small-angle neutron scattering captures nearly an additional decade in q. The absolute intensity in cm^{-1} differs due to differences in x-ray vs. neutron scattering contrast of the PBX constituents TATB/Kel-F 800.

In the left pane of figure 3, the void distributions derived with USAXS are presented, and are similar, but not identical, to results obtained previously on LX-17[1, 2]. The total void volume derived from the small angle scattering before ratcheting was 1.3% (USAXS) and 1.3% (USANS) while after ratcheting, 2.7% (USAXS) and 2.2%(USANS). In this left pane, an area is highlighted from about 1 to 15 microns in size. This area is shown in the right pane, and size distributions from both the USAXS and the USANS are presented for both pre- and post-ratchet LX-17. Near the upper sensitivity limit of USAXS (~ 2 μm), USANS shows 0.4% of the volume is voids larger than 1 μm, with 0.1% of this volume from voids larger than 2 μm. For comparison, USAXS shows 0.2% (> 1 μm) and less than 0.1% (> 2 μm). After ratchet growth, the void volume attributable to these sizes using USANS increases to 0.6% (> 1 μm) and 0.2% (> 2 μm). USAXS reports 0.4% (> 1 μm) and 0.1% (> 2 μm). We conclude that USANS is reporting incrementally more voids larger than 1 μm compared to USAXS, but that the results still do not completely account for the decrease in density seen in LX-17 after ratchet growth[1]. This indicates the existence of voids with sizes larger than 10 microns both existing in LX-17 and becoming more prevalent after temperature cycling. Based on density vs. scattering measurements, larger voids encompass roughly 0.5 % of the total volume in these particular samples.

Tomography was used to obtain an estimate of void volume distribution for voids with diameter between about 3 microns and 15 microns. Voids were found by using an inscribed rectangular box volume of 250 microns by 250 microns by 430 microns from within the reconstructed 0.4 mm diameter by 0.8 mm tall cylinder, the voxels with μ sufficiently close to zero with connectivity constituted a void; volumes were determined by counting these connected voxels. The diameters of each void were estimated by using the simple relation for spherical particles $d = \sqrt[3]{6V/\pi}$. Although simplistic, this is analogous to the method used for scattering techniques, in that a form factor for spheres is assumed. Based on these assumptions, the void volume distribution obtained from tomography is presented in the right pane Figure 3 (along with USAXS and USANS derived distributions), with diameters ~ 3 microns and larger. The integrated volume from the tomography voids is 0.37% of the total volume.

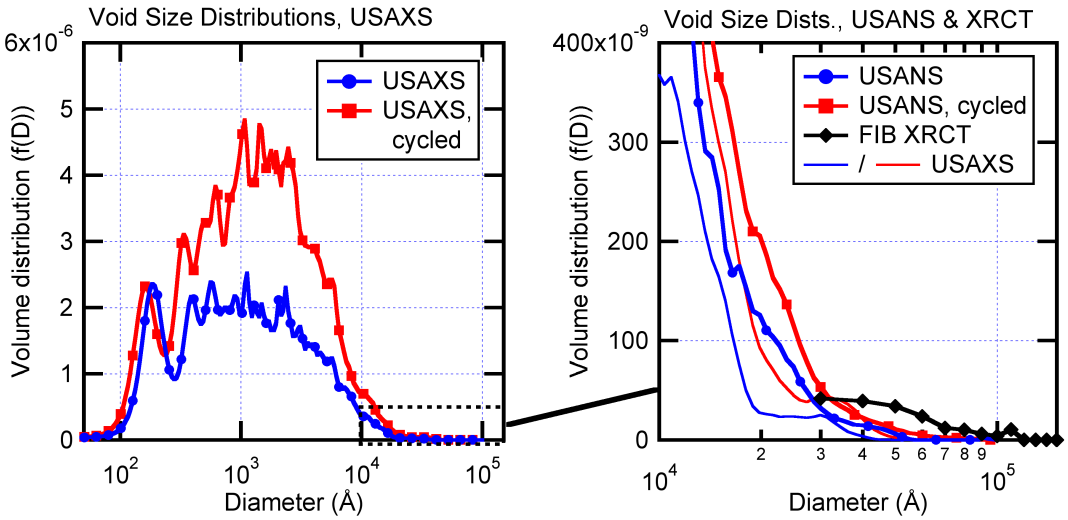

Figure 3: Left pane: Maximum-entropy derived size distributions from the USAXS data. Right pane: An inset view from the left pane that includes and emphasizes the USANS and FIB-XRCT void volume distributions.

This void volume is slightly less than, and matches, perhaps fortuitously well, the roughly 0.5% void volume not accounted for using USAXS. Previously, on a number of different samples, USAXS accounted for about 1.5% of the voids determined with density measurements to be 2.0%[1]. In this small sample, voids 3-15 microns make up nearly 0.4% of the volume. Although this is a remarkable match, there are weaknesses in the methods used for this estimation. First, the small inscribed volume may not be completely representative of bulk LX-17, especially given the variations in composition on the 1 mm

scale presented later in this report. Voxel counting is not particularly accurate due to phase effects in the imaging and uncertainty for boundary locations. Further, this sample was a separate pressing, known to cause some variation, while USANS and USAXS presented here were from exactly the same samples. Even with these experimental uncertainties, this technique allows us to image voids with sizes from a few microns to a few 10's of microns, and despite the small sampling, their volume does capture and represent a significant portion of the voids not accounted for when using scattering techniques.

Figure 4 presents synchrotron-based x-ray computed tomography reconstructed slices, 9 microns thick, acquired about 12 mm from the top of the sample. The leftmost pane a) presents a fully-pressed, 98.6% TMD sample, and is a reference for what one might expect for the optimal microstructure of LX-17 as seen previously[10].

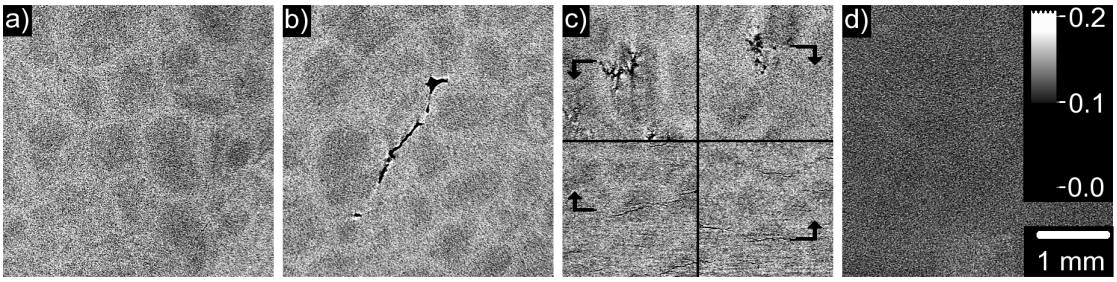

Figure 4: a) Typical LX-17 microstructure, with TATB rich areas surrounded by binder-rich boundaries, overall density is 1.92 g/cc or 98.6% TMD. b) A large void within the LX-17, apparently at prill boundaries. c) Incompletely pressed LX-17 at 1.89 g/cc or 97.0% TMD. Voids appear in the reconstructed slices (upper panes) and are predominantly within the prill particle. Orthogonal views (lower panes) reveal these irregular cracks are generally two-dimensional and are parallel to the pressing face. Voids that appear in both views are annotated. d) TATB-based explosive using a commercial Cytop binder rather than Kel-F 800; the microstructural variation is less pronounced than LX-17. The overall darker appearance is due to the lighter elements used in the Cytop binder.

The scale at the right of the figure represents x-ray attenuation coefficients, with units of mm^{-1}. The expected attenuation coefficients for the constituents and composite are as follows: TATB, $C_6H_6N_6O_6$ at 1.93 g/cm^3: 0.11 mm^{-1}; Kel-F 800, $C_8H_2F_{11}Cl$ at 2.14 g/cm^3: 0.31 mm^{-1}, and finally, the LX-17 composite of 92.5% TATB, 7.5% Kel-F 800: 0.12 mm^{-1}[20]. Cytop on has an attenuation coefficient of about 0.16 mm^{-1}. The Kel-F 800 rich regions are visible as lighter boundary regions while TATB rich regions are a darker hue, and have previously been attributed to a variation in binder content ranging from 5.9% in binder

poor regions to 8.5% in binder rich regions[10]. These areas arise from the formulation of the Kel-F 800 with the TATB, which results in mm-sized beads or "prills" of LX-17 molding powder suitable for pressing.

Two classes of larger voids in LX-17 have been identified. They occur both at prill particle boundaries and within the interior of the prill, and they form under very different conditions. The first type of larger (>20 micron) voids are located at prill particle boundaries and occur in even fully pressed materials. Perhaps the largest such void imaged in thus far is presented in Figure 7. The void presented is one continuous structure, but for simplicity and clarity, only one 9 micron thick reconstructed slice is presented. The void clearly lies between prills; this is particularly evident in the upper right portion of the void that is at the intersection of a number of prill particle boundaries. Apparently, in some cases, pressing does not deform the prill particles sufficiently to result in full density and fully consolidated material. Although the origin and mechanism of formation of these voids is not fully understood, feasible explanations could be that in a sufficiently binder-rich region, a gas bubbles are trapped and sealed within the explosive during unevacuated pressing, or that the heat soak is not sufficient for the binders of these particular prill particles to become fully plastic while deforming into conforming shapes required for completely consolidated material. Note the presented void represents the extreme case where the void is approximately two millimeters long, and that these voids represent only a small portion of the total volume. Preliminary indications, by sorting through the reconstructed volume about 3 cubic centimeters of fully pressed material, found similar but much smaller prill boundary voids, typically on the order of 100's of microns in length. These occurred at about 3-4 voids per cubic centimeter in these particular samples. At such frequency, the bulk void volume contribution will typically be less than 0.1%. (As an example, a 100 micron diameter tube 2 mm long, similar in size to this very large void, in one cm^3 of explosive represents about 0.006% of the bulk volume.) Quantitative determination of size and frequency of such defects will be determined in future work.

Figure 4, pane c) presents a slice from a specimen intentionally pressed to lower density, giving insight into the mechanisms of consolidation and compaction of the LX-17 during pressing. The top panes are slices similar to panes a) and b); the lower panes illustrate slices orthogonal to these top panes. The lines of voxels that are common to both slices is indicated by arrows in both panes. The panes show incomplete consolidation results in a highly inhomogeneous microstructure. Both views show voids predominantly within the prill interior TATB-rich and binder-poor regions. Two particular prill particles are annotated in

the figure. The voids are irregularly shaped, nearly flat cracks in the material. This sample was pressed with two dwells, rather than three, and is thus representative of an intermediate state during pressing. The prill particles deform and meet at the binder rich prill interfaces in the initial stages of pressing; this prill deformation and associated tension causes cracking and void appearance within the interior of the particles. It seems that these fractures are healed in the final stages of pressing, however, even in fully consolidated parts that have been cut to small sizes, evidence of similar (although much thinner) two dimensional cracks, parallel to the pressing face, appeared in the material. The fractional volume represented by these cracks is consistent with the lower observed density. Simply counting low intensity voxels, about 0.7% of the volume in this particular uniaxially pressed part are these voids. This number accounts for a large fraction of the 1.5% difference in intensity between the fully-pressed (~98.6% TMD) and partially pressed (~97% TMD) material.

Figure 4, pane d presents a PBX of TATB with a Cytop binder[2, 8]. This binder has performed well in inhibiting ratchet growth and the associated changes to hot-spot voids[2]. The explosive also appears to show better homogeneity than Kel-F 800 based materials, a step towards next generation TATB-based materials.

Conclusions

TATB-based explosives have been investigated on multiple length scales, using ultra-small angle x-ray scattering, ultra small angle neutron scattering, and x-ray computed tomography. USAXS, used to image the smallest voids including hot-spot voids from hundreds of nanometers to a few microns, shows an increase in both the number of these voids and a shift in the size distribution towards larger sizes with temperature cycling. Not all of the voids are interrogated with USAXS alone; USANS, able to probe structures up to about 10 microns, shows incremental additional void volume (a few tenths of a percent) beyond the sensitivity of USAXS.

For still larger structures in TATB-based explosives, X-ray computed tomography has been used to investigate LX-17 on two length scales. Voids from a few microns to about 20 microns have been imaged in a small, 0.4 mm diameter sample, and the voids are consistent with, and account for much of the voids that cannot be seen with USAXS or USANS.

The location and nature of two very different classes of large voids has been determined using synchrotron-based x-ray computed microtomography. The first type of void occurs at prill particle boundaries, with relatively smooth interfaces, and typically has length dimensions from 100's of microns up to 1-2 mm. These appear sparsely even in fully

consolidated pressings; in the samples investigated at a rate of 3-4 voids per cubic centimeter, but account for a small portion (<0.1%) of the total volume.

The second class of void typically occurs within the TATB-rich and Kel-F 800 poor prill particle interiors. They are evident in all specimens intentionally not pressed to full density. These voids are highly irregular, roughly two dimensional, and are approximately coplanar with the face of the pressing piston. In this case, prill boundaries consolidate, but deformation of prills causes fracture in the binder-poor interior. Further, they represent a volume that accounts for a large fraction of the difference in density with fully pressed materials.

Binders that have previously been shown to be superior to Kel-F 800 in minimizing void changes also exhibit a more uniform microstructure, a step towards next-generation TATB-based explosives.

These data are an important step to understanding microstructural mechanisms that affect the mechanical properties of LX-17, and provide complete a comprehensive characterization of the structure of LX-17 from nanometers to centimeters that can be used as empirical input to computational models of detonation, and in determining the relationship between voids and microstructure to detonation properties.

Acknowledgements

The authors thank Lisa Lauderbach, John Kinney, Nick Teslich, Jonathan R. I. Lee, Tony van Buuren, and Dan Scheberk(LLNL); Alastair MacDowell, Eric Schaible, and James Nasiatka (LBNL) John Barker (NIST), and Jan Ilavsky (Argonne), for assistance in acquiring these data. This work performed under the auspices of the U.S. Department of Energy by Lawrence Livermore National Laboratory under Contract DE-AC52-07NA27344. Use of the Advanced Photon Source was supported by the U. S. Department of Energy, Office of Science, Office of Basic Energy Sciences, under Contract No. DE-AC02-06CH11357. The Advanced Light Source is supported by the Office of Science, Office of Basic Energy Sciences, of the U.S. Department of Energy under Contract No. DE-AC02-05CH11231. This work used neutron research facilities at the National Institute of Standards and Technology, U. S. Department of Commerce, supported by the National Science Foundation under Agreement No. DMR-0454672.

References

1. Willey, T.M., et al., *Changes in Pore Size Distribution upon Thermal Cycling of TATB-based Explosives Measured by Ultra-Small Angle X-ray Scattering.* Propellants, Explosives, Pyrotechnics, 2006. **31**(6): p. 466-471.
2. Willey, T.M., et al., *The Microstructure of TATB-based Explosive Formulations Monitored During Temperature Cycling Using Ultra-small Angle X-ray Scattering.* Propellants Explosives Pyrotechnics, 2009. **in press**.

3. Belmas, R. and J.P. Plotard, *Physical Origin of Hot-Spots in Pressed Explosive Compositions.* Journal De Physique Iv, 1995. **5**(C4): p. 61-87.
4. Tarver, C.M., S.K. Chidester, and A.L. Nichols, *Critical conditions for impact- and shock-induced hot spots in solid explosives.* Journal of Physical Chemistry, 1996. **100**(14): p. 5794-5799.
5. Hamate, Y. and Y. Horie, *Ignition and detonation of solid explosives: a micromechanical burn model.* Shock Waves, 2006. **16**(2): p. 125-147.
6. Rizzo, H.F., J.R. Humphrey, and J.R. Kolb, *Growth of 1,3,5-Triamino-2,4,6-Trinitrobenzene (Tatb) .2. Control of Growth by Use of High Tg Polymeric Binders.* Propellants and Explosives, 1981. **6**(2): p. 27-36.
7. Rizzo, H.F., J.R. Humphrey, and J.R. Kolb, *Growth of 1,3,5-Triamino-2,4,6,-Trinitrobenzene (Tatb) .2. Control of Growth by Use of High-Tg Polymeric Binders.* Propellants and Explosives, 1981. **6**(3): p. 57-62.
8. Gee, R.H., et al., *Molecular dynamics investigation of adhesion between TATB surfaces and amorphous fluoropolymers.* Macromolecules, 2007. **40**(9): p. 3422-3428.
9. Gee, R.H., A. Maiti, and L.E. Fried, *Mesoscale modeling of irreversible volume growth in powders of anisotropic crystals.* Applied Physics Letters, 2007. **90**(25): p. 254105.
10. Kinney, J.H., T.M. Willey, and G.E. Overturf. *On the Nature of Variations in Density and Composition within TATB-based Plastic Bonded Explosives*. in *Proceedings of the 13th International Detonation Symposium*. 2006. Norfolk, VA, USA.
11. Roeske, F., et al., *Cutting and Machining Energetic Materials with a Femtosecond Laser.* Propellants, Explosives, Pyrotechnics, 2003. **28**(2): p. 53-57.
12. Ilavsky, J., et al. *Versatile collimating crystal stage for a Bonse-Hart USAXS instrument*. in *9th International Conference on Synchrotron Radiation Instrumentation (SRI 2006)*. 2006. Daegu, South Korea: AIP Conference Proceedings.
13. Ilavsky, J., et al., *Effective pinhole-collimated ultrasmall-angle x-ray scattering instrument for measuring anisotropic microstructures.* Review of Scientific Instruments, 2002. **73**(3): p. 1660-1662.
14. Long, G.G., et al. *The Ultra-Small-Angle X-ray Scattering Instrument on UNICAT at the APS*. in *Synchrotron Radiation Instrumentation: SRI 99: 11th U.S. National Conference*. 1999: AIP Conference Proceedings.
15. Barker, J.G., et al., *Design and performance of a thermal-neutron double-crystal diffractometer for USANS at NIST.* Journal of Applied Crystallography, 2005. **38**(6): p. 1004.
16. Kline, S.R., *Reduction and Analysis of SANS and USANS Data Using Igor Pro.* Journal of Applied Crystallography, 2006. **39**(6): p. 895.
17. Ilavsky, J. and P.R. Jemian, *Irena: tool suite for modeling and analysis of small-angle scattering.* Journal of Applied Crystallography, 2009. **42**(42): p. in press.
18. Robin, D., et al., *Superbend upgrade on the Advanced Light Source.* Nuclear Instruments & Methods in Physics Research Section a-Accelerators Spectrometers Detectors and Associated Equipment, 2005. **538**(1-3): p. 65-92.
19. Wang, Y.X., et al., *A high-throughput x-ray microtomography system at the Advanced Photon Source.* Rerview of Scientific Instruments, 2001. **72**(4): p. 2062-2068.
20. http://www-cxro.lbl.gov/.